

DOCTORAL THESIS

Thesis Title

Author:

Ana ANDRES-ARROYO

Supervisor:

Dr. First LAST

A thesis submitted in fulfilment of the requirements for the degree of
Doctor of Philosophy



School of Physics, Faculty of Science

September 2018

Dedicated to someone.

“Fancy Quote”

Author

Abstract

School of Physics, Faculty of Science, UNSW Australia

Doctor of Philosophy

Thesis Title

by Ana ANDRES-ARROYO

Write your abstract here .

Acknowledgements

The acknowledgements and the people to thank go here, don't forget to include your project advisor...

Contents

Dedicatory	iii
Quotation	v
Abstract	vii
Acknowledgements	viii
Contents	ix
List of Figures	xi
Abbreviations	xiii
Physical Constants	xv
Symbols	xvii
1 Introduction	1
1.1 Section title	2
1.2 Compiling instructions	2
1.3 References	2
2 Using Fourier transform phase for the measurement of radial velocity	3
2.1 Phase analysis of Fourier transform for the measurement of line shift . . .	5
2.1.1 Translation property of Fourier transform	5
2.1.2 Intuitive explanation	6
2.1.3 Practical Use	6
2.1.4 Initial tests	7
2.1.5 Further tests	10
2.1.6 Cut-off frequency	12
2.1.7 Conclusion	13
2.2 Using the Fourier transform to probe line deformation	14
2.2.1 Theory	14
2.2.2 SOAP simulations	15
2.2.3 Fourier phase spectrum analysis	16
2.2.3.1 RV_{FT}	16
2.2.3.2 $RV_{\text{FT,H}}$ and $RV_{\text{FT,L}}$	17

2.2.4	Jitter model	20
2.2.5	Testing the recovery of jitter	21
2.2.6	Planetary radial velocity recovery	23
2.2.7	End-to-end simulations	25
2.2.7.1	Stellar jitter as strong as planetary signal	26
2.2.7.2	Planetary signal dominates	28
2.2.7.3	Stellar jitter only	29
2.3	Fourier transform with real observations	29
2.3.1	HD189733: Rossiter–McLaughlin effect as jitter	29
	Remarks	31
2.3.2	Examples 2	32
2.3.3	Example 3	32
2.4	References	32

List of Figures

1	Introduction	1
2	Using Fourier transform phase for the measurement of radial velocity	3
2.1	Translation property of Fourier transform	7
2.2	100 shifted HARPS-like line profiles	8
2.3	Fourier transform of 100 shifted line profiles	8
2.4	Radial velocity recovery	10
2.5	Low-pass and high-pass filters	11
2.6	Low-pass and high-pass radial velocities	12
2.7	Fourier transform of a line profile in a complex plane	13
2.8	Deformed line profile	15
2.9	Fourier transform of deformed line profile	16
2.10	Apparent RV of deformed line profile	17
2.11	Low-pass and high-pass filters	18
2.12	Fourier transform in response to line deformation	19
2.13	Scaling the low-pass and high-pass Fourier transformed radial velocities .	19
2.14	Jitter model	23
2.15	Corner plots of MCMC	26
2.16	Planet recovery ($A = 2$ m/s)	27
2.17	Histogram of recovered orbital parameters ($A = 2$ m/s)	27
2.18	Planet recovery ($A = 20$ m/s)	28
2.19	Histogram of recovered orbital parameters ($A = 20$ m/s)	28
2.20	Histogram of recovered orbital parameters of null planets	29
2.21	Demo: Rossiter–McLaughlin effect	30
2.22	HD189733: removal of Rossiter–McLaughlin effect as jitter	31

Abbreviations

2D Two-Dimensional

3D Three-Dimensional

Physical Constants

Speed of Light c = $2.997\,924\,58 \times 10^8 \text{ ms}^{-\text{s}}$ (exact)

Constant Name Symbol = Constant Value (with units)

Symbols

f	focal length	mm or cm
H	heating	K/W
I	intensity	a.u.
k	trap stiffness	pN/ μ m/mW
n	refractive index	—
P	power	mW
T	temperature	$^{\circ}$ C or K
ε	permittivity	???
κ	trap stiffness	pN/ μ m/mW
λ	wavelength	nm
μ	permeability	???
σ	cross section	???
θ	tilt angle	degrees or radians

¹Chapter 1

Introduction

1.1	Section title	2
1.2	Compiling instructions	2
1.3	References	2

1.1 Section title

Always put labelthsection after each section so the page headers work. [?]

This is a test.

1.2 Compiling instructions

1. make the main file the masted document: options -i make current file masted document
2. Quick build from anywhere (because it quick builds from the master document
3. BibTex from the chapter file (disable the master document option for this and do it from "normal mode")
4. Quick build 3 times (from the master document): 1 for the text, 2 for the references and labels, 3 for the bibliography backreferencing.

1.3 References

¹ Chapter 2

Using Fourier transform phase for the measurement of radial velocity

2.1	Phase analysis of Fourier transform for the measurement of line shift	5
2.1.1	Translation property of Fourier transform	5
2.1.2	Intuitive explanation	6
2.1.3	Practical Use	6
2.1.4	Initial tests	7
2.1.5	Further tests	10
2.1.6	Cut-off frequency	12
2.1.7	Conclusion	13
2.2	Using the Fourier transform to probe line deformation	14
2.2.1	Theory	14
2.2.2	SOAP simulations	15
2.2.3	Fourier phase spectrum analysis	16
2.2.3.1	RV_{FT}	16
2.2.3.2	$RV_{FT,H}$ and $RV_{FT,L}$	17
2.2.4	Jitter model	20
2.2.5	Testing the recovery of jitter	21
2.2.6	Planetary radial velocity recovery	23
2.2.7	End-to-end simulations	25
2.2.7.1	Stellar jitter as strong as planetary signal	26

2.2.7.2	Planetary signal dominates	28
2.2.7.3	Stellar jitter only	29
2.3	Fourier transform with real observations	29
2.3.1	HD189733: Rossiter–McLaughlin effect as jitter	29
	Remarks	31
2.3.2	Examples 2	32
2.3.3	Example 3	32
2.4	References	32

This chapter introduces a new method for measuring radial velocities. Specifically, it uses the Fourier transform of a line profile (or cross-correlation profile) to try and distinguish between the effects of a bulk shift in that profile (i.e. a radial velocity shift of the profile), opposed to a change in the line profile shape which can produce an apparent radial velocity shift. We examine the impact on the Fourier transformed components of a line profile of both bulk line shifts, and line profile deformations, with the aim of developing tools to distinguish between these two cases.

2.1 Phase analysis of Fourier transform for the measurement of line shift

2.1.1 Translation property of Fourier transform

The translation of a function (in our case a spectral line profile) can be examined in both its original real space, and in its Fourier transformed space. Because Fourier techniques are often used to handle time domain data, this shift in real space can be variously considered described as either time shifting or translation. In this chapter we will use “time shifting”, “translation” and “velocity shifting” interchangeably to refer to a shift of a function in real space. We will refer to Fourier transformed functions as being in the “frequency domain” regardless of whether they have actual dimensions of 1/time, 1/length or 1/velocity.

Let us consider a function $h(x)$ be a signal $f(x)$ delayed (or shifted) by an amount x_0 :

$$h(x) = f(x - x_0). \quad (2.1)$$

In the frequency domain, we will then have

$$\hat{h}(\xi) = e^{-2\pi i x_0 \xi} \hat{f}(\xi), \quad (2.2)$$

where the circumflex denotes the Fourier transform of a function. $\hat{h}(\xi)$ and $\hat{f}(\xi)$ will therefore differ by a frequency dependent phase angle:

$$\Delta\phi(\xi) = -2\pi x_0 \xi, \quad (2.3)$$

while the power spectral density will remain unchanged (as $|e^{-2\pi i x_0 \xi}|^2 = 1$).

2.1.2 Intuitive explanation

The translation property of the Fourier transform follows mathematically from the nature of the transform. A (perhaps) more intuitive way to see this is that since the Fourier transform is defined

$$\hat{f}(\xi) = \int_{-\infty}^{\infty} f(x) e^{-2\pi i x \xi} dx, \quad (2.4)$$

it decomposes the function $f(x)$ into a frequency representation $\hat{f}(\xi)$, such that the function $f(x)$ is expressed as the sum of *all* the orthogonal basis $e^{2\pi i x \xi}$ times a set of their components $\hat{f}(\xi)$ (i.e. by the inverse Fourier transform):

$$f(x) = \int_{-\infty}^{\infty} \hat{f}(\xi) e^{2\pi i x \xi} d\xi. \quad (2.5)$$

This means that shifting $f(x)$ by x_0 is equivalent to shifting *all* the orthogonal basis functions by x_0 , which becomes $e^{2\pi i (x-x_0)\xi} = e^{2\pi i x \xi} \cdot e^{-2\pi i x_0 \xi}$. This is how the $e^{-2\pi i x_0 \xi}$ term in Eq. 2.2 arises – it quantifies this phase difference.¹

The fact that the power spectrum density remains the same can also intuitively seen, because shifting the signal as a whole doesn't add or remove any frequency information.

2.1.3 Practical Use

From Eq. 2.3, we see that the phase shift $\Delta\phi(\xi)$ is proportional to the frequency ξ with a constant gradient or slope²

$$\frac{d(\Delta\phi)}{d\xi} = -2\pi x_0 \quad (2.6)$$

Obtaining this (in principle) is straightforward via a simple linear regression model fit to a plot of $\Delta\phi(\xi)$ versus ξ (see e.g. Fig. 2.1), so that

$$x_0 = -\frac{1}{2\pi} \frac{d(\Delta\phi)}{d\xi} \quad (2.7)$$

¹For a simplified vision bridging a shift of the signal in the time domain and a phase difference in the frequency domain, imagine any real continuous function is a sum of sines and cosines. Changing the phase angle in the sines and cosines results in shifts in the function.

²We use Δ to refer to the phase difference between a shifted line profile and a unshifted / referenced line profile, while the derivative to refer to the response of $\Delta\phi$ to ξ .

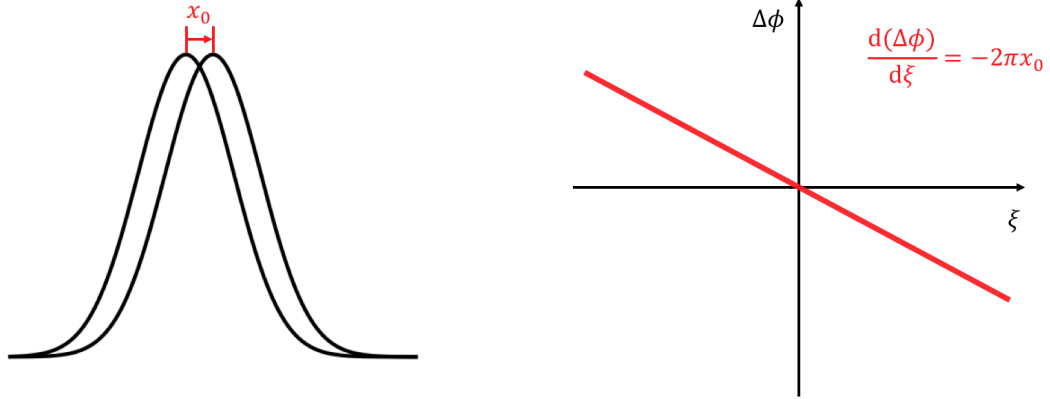


Fig. 2.1: The left panel shows a signal (or a spectral line profile in the following context) shifted by an amount x_0 . The right panel is the differential phase spectral density diagram (i.e. differential phase spectrum). The model shows a perfectly linear correlation between $\Delta\phi(\xi)$ and ξ with the constant slope $-2\pi x_0$.

By analogy with the definition of power spectral density, we describe $\phi(\xi)$ the “phase spectral density” and hence $\Delta\phi(\xi)$ the “differential phase spectral density”.

In principle then, an analysis of the phase shift in the frequency domain of the Fourier components of a line profile will provide a means of measuring a bulk line shift in real space.

2.1.4 Initial tests

We performed an initial test to determine whether we can correctly recover known shifts of a line profile from an analysis of the phase shift in the frequency domain of the Fourier transform of shifted line profiles.

We generated a spectral line profile based on the cross-correlation function of observed HARPS spectra with the software SOAP 2.0 [1]. This was replicated 100 times, with a very small amount of noise (equivalent to a S/N = 10,000) injected in each of the line profiles. These profiles were then subjected to radial velocity shifts evenly spaced between 0 and 10 m/s (Fig. 2.2).

The Fourier transform of these 100 spectral line profiles divides the information into two parts: (1) the power spectra (Fig. 2.3a) and (2) the phase spectra (shown in Fig. 2.3b as the differential phase spectra relative to the phase spectrum for the unshifted line profile).

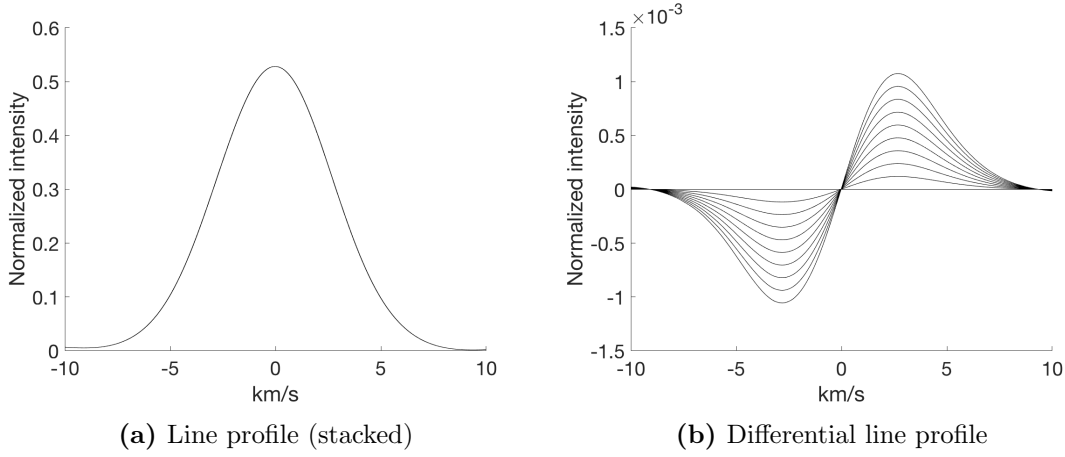


Fig. 2.2: (a) the shifted line profiles plotted on top of each other, showing that the ± 0 -10 m/s shifts are very small compared to the line profile width. (b) the shifted line profiles with the unshifted line profile subtracted from each. Note that for the sake of clarity, the differential line profiles are plotted noise-free and only 10 out of 100 profiles are presented.

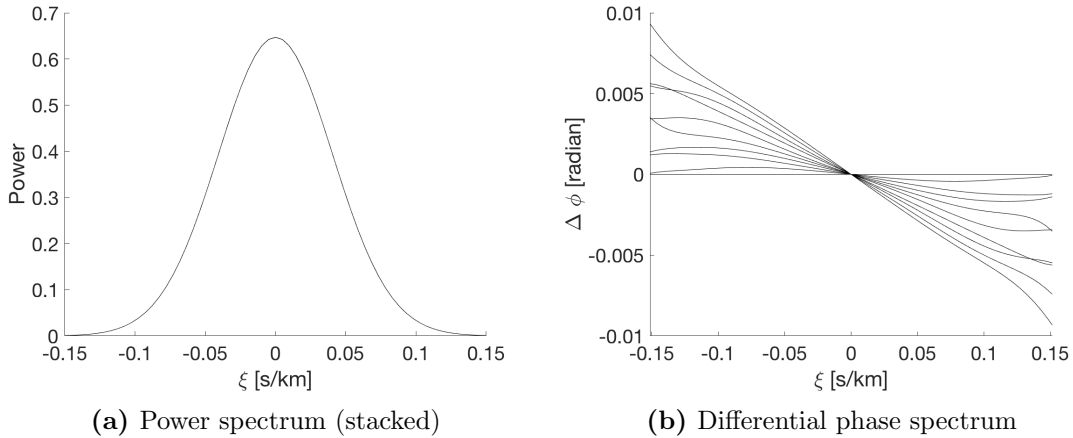


Fig. 2.3: The Fourier transform of these shifted line profile divides the information in each into (a) their power spectra and (b) their phase spectra (here plotted differential compared to that of the unshifted profile). A line shift in the time domain produces an unchanged power spectrum in the frequency domain. It does, however, produce phase shift which we see as linear trends in the differential phase spectra as a function of frequency. Note that for demonstration clarity, only 10 out of 100 differential phase spectra are presented.

We see that most Fourier transform information is concentrated towards the centre of the power spectrum (i.e. the lower frequency range). The differential phase spectra are expected linear (as Fig. 2.1 demonstrated). Its deviation from linearity comes from the noise that we injected, which will be discussed later.

The slope of each differential phase spectrum indicates the shift of each line profile relative to the unshifted line profile. It should be weighted by the amplitude of the power, meaning the lower frequencies are higher weighted. We therefore calculate the radial velocity shift for each shifted line profile using two methods:

1. the RV_{FT} using Eq. 2.7, weighted by the power spectrum
2. the RV_{Gaussian} as traditionally measured from the line centroid by fitting a Gaussian to each line profile.

We can then compare the results with the (known) input line shift where we see the expected strong 1:1 correlation (Fig. 2.4)³. The root-mean-square (rms) of the residuals (or interchangeably used as standard deviation when the mean is zero) are both $\sigma_{\text{FT}} = \sigma_{\text{Gaussian}} = 0.08$ m/s, identical up to two decimal places, indicating the expected radial velocities are consistently reduced. In fact, the almost overlapping residual in Fig. 2.4 means that the two methods are so coherently different from the input radial velocity (by a small amount), concludes that such a deviation comes from the photon noise intrinsic to the line profile rather than the methods themselves.

CGT: How do these compare which what you'd expect from the S/N and the intrinsic line width (should say at some int what the intrinsic line width is).

³The line of best fit of a linear regression model presents a slope of 1.003 ± 0.006 with 95% confidence bounds.

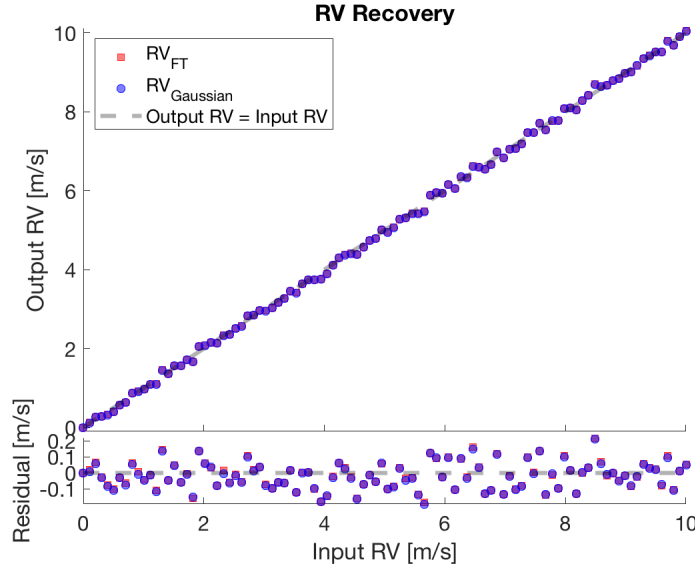


Fig. 2.4: Radial velocity recovery of line shifts with both methods: Fourier transform and Gaussian fit. Both results are highly consistent with each other. Error-bars are not plotted for clarity.

2.1.5 Further tests

Let's recall the justification of measuring a line shift in its Fourier space – the shifting of a line (or a function), when viewed as shifting the sum of its Fourier basis functions (or any other basis functions), has equally the same amount of shift on every basis function, which can be measured as a phase shift in the Fourier phase spectrum. That is to say, utilising only part of the phase spectrum will also return the correct amount of shift of a line profile, although it is more likely to be affected by noise. The motivation of this practice will be discussed in §2.2 when it comes to line profile deformations, while we simply lay out the tests in this subsection.

We choose to divide the whole frequency range into two parts (Fig. 2.5) – the lower frequency range (i.e. apply a low-pass filter) and the higher frequency range (i.e. apply a high-pass filter). The dividing frequency ξ_{HL} is chosen such that both the lower and higher frequency ranges take up half of the power spectrum:⁴

$$\int_0^{\xi_{HL}} P(\xi) d\xi = \int_{\xi_{HL}}^{+\infty} P(\xi) d\xi, \quad (2.8)$$

⁴In practice, a cut-off frequency applies to the upper boundary of the high-pass filter. Frequencies higher than the cut-off frequency hardly contributes to the shape of the line profile as the power goes to 0, and they can be impacted by noise in an unpredictable way, although they are weighted by the nearly-zero power.

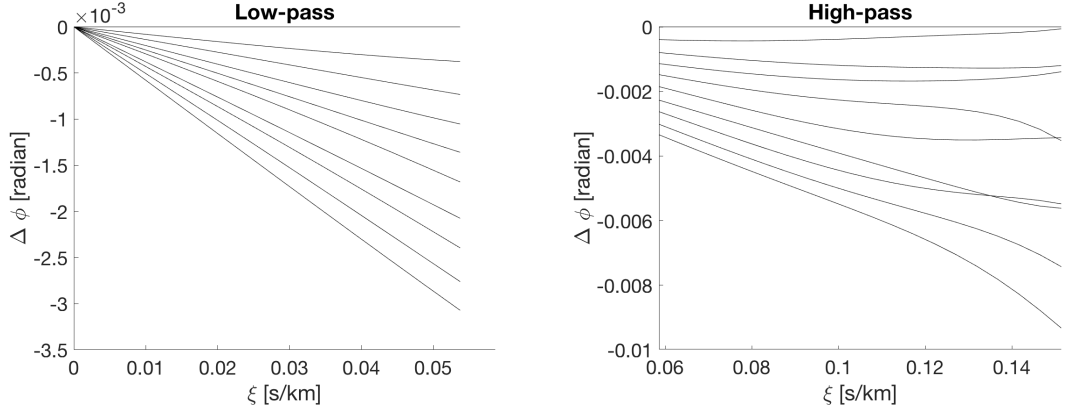


Fig. 2.5: Differential phase spectrum as shown in Fig. 2.3b sub-divided into lower frequency range and higher frequency range. Only the non-negative ranges are plotted.

assuming the integration of power spectrum is a measurement of the amount of “information”, so that in a noise-free circumstance, we would put equal trust on the radial velocities obtained from the lower and higher frequencies. In the following, we use $RV_{\text{FT,L}}$ and $RV_{\text{FT,H}}$ to represent these two radial velocities.

Similar to Fig. 2.4 where we make use of the full range of frequencies, Fig. 2.6 also presents a good 1:1 alignment between $RV_{\text{FT,L}}$, $RV_{\text{FT,H}}$ and the input radial velocity⁵. The scatter of the residuals are $\sigma_{\text{FT,L}} = 0.11$ m/s and $\sigma_{\text{FT,H}} = 0.43$ m/s, seemingly contradicting with the expectation that equal amount of “information” from which $RV_{\text{FT,L}}$ and $RV_{\text{FT,H}}$ are derived should deliver the same amount of scatter. The answer lies in the impact of noise (§2.1.6) – higher frequency modes are more likely to be subjected to line deformations arising from stochastic behaviours, such as photon noise, stellar variability...

⁵The line of best fit presents a slope of 1.002 ± 0.007 for $RV_{\text{FT,L}}$ and 0.977 ± 0.029 respectively, with 95% confidence bounds.

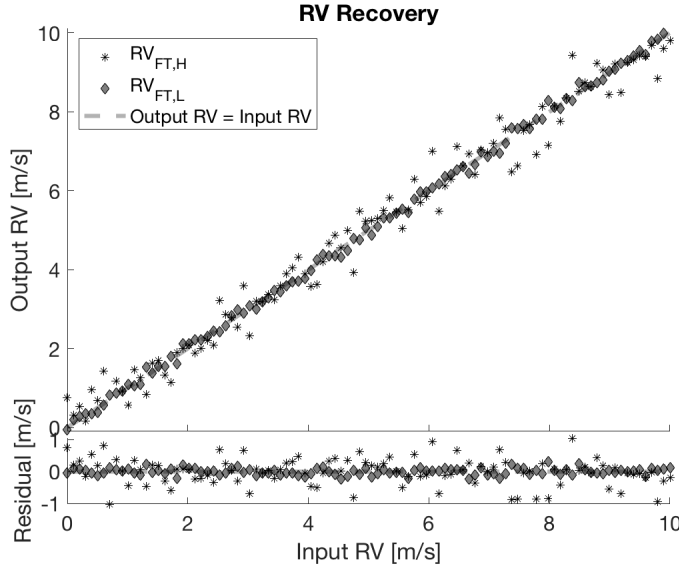


Fig. 2.6: Radial velocity recovery of line shifts with low-pass and high-pass filters. Errorbars are not plotted for clarity.

2.1.6 Cut-off frequency

We briefly mentioned in §2.1.4 that the deviation from linearity in the differential phase spectrum arises from the photon noise injected in the simulated line profile, and in §2.1.5 that introducing a cut-off frequency in the upper boundary avoids dealing with excessive noise. This can be explained with the Fourier transformed line profile $\hat{h}(\xi)$ in a complex plane (also known as the Argand plane; Fig. 2.7). What we see is $\hat{h}(\xi)$ literally plotted on the complex plane – of each complex number $\hat{h}(\xi)$, the argument returns the phase angle and the square of the absolute value returns the power, for that particular frequency ξ . For larger powers (i.e. $\hat{h}(\xi)$ far from the origin), the presence of noise hardly alters the phase angle; for lower powers (i.e. $\hat{h}(\xi)$ distributed in the vicinity of the origin), a slight displacement of $\hat{h}(\xi)$ in the complex plane means a considerable change in the phase angle. It justifies using the Fourier transform spectral power to be the weight of each frequency, and introducing a cut-off frequency when making a linear fit of the differential phase spectrum.

Another possible reason for introducing the cut-off frequency is the periodicity of the basis functions in a Fourier transform. The basis function $e^{-2\pi i x_0 \xi}$ repeats itself at the period of $1/\xi$, making measuring the shift longer than the order of $1/\xi$ degenerate because $x_0 + k/\xi$ for $k \in \mathbb{Z}$ will give the same results. However, this is very unlikely the case that we may encounter. In the test examples above, the cut-off frequency is

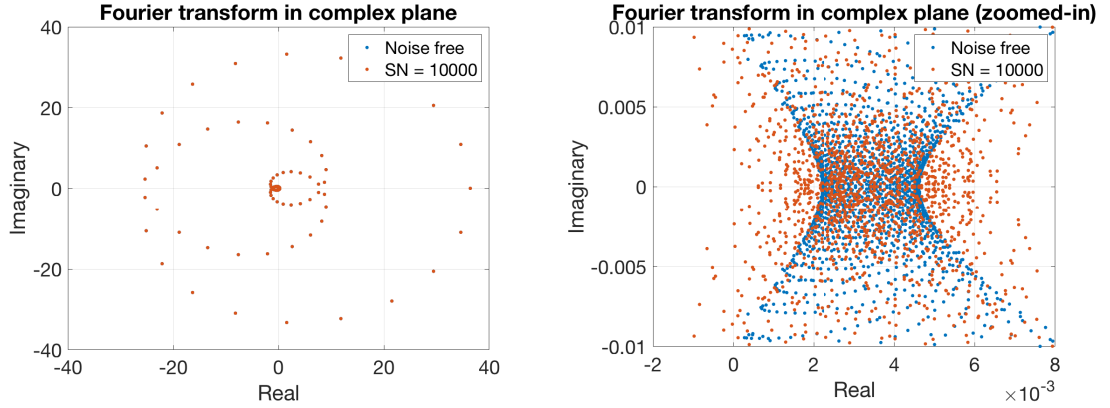


Fig. 2.7: The Fourier transform of a line profile in a complex plane. The right figure is a zoom-in of the left near the origin.

$\xi = 0.15$ s/km, corresponding to the period of $1/\xi \sim 6.7$ km/s, way larger than the radial velocities induced by planets at m/s amplitudes.

2.1.7 Conclusion

In this section, we have introduced a new method for measuring radial velocities – Fourier phase spectrum analysis. The tests that we have made based on shifting a simulated line profile confirm our expectation that using the differential Fourier phase spectrum, it is possible to measure a radial velocity to similarly high precision. This provides an alternative to the traditional means of obtaining the radial velocities via centroiding the line profile in real space.

In a broader context, this method will be applicable to measuring shifts of any pattern, and can be extended to higher dimensions. In this thesis, we primarily focus on its use to measure radial velocity shifts in spectral line profiles, and especially whether the Fourier transform phase velocity is more robust against the influence of changes in line deformation than traditional techniques.

2.2 Using the Fourier transform to probe line deformation

In § 2.1, we have tested that the Fourier phase spectrum analysis correctly measures the actual line profile shifts due to a bulk motion of the emitting star. In this section, we wish to test whether this method is more robust against spurious apparent radial velocity shifts produced by changes in the line profile shape in an emitting stars.

2.2.1 Theory

For a shift of a line profile by a small amount x_0 , the same shift x_0 applies to *all* of its basis functions. As for line deformation due to stellar variability, x_0 becomes frequency dependent ⁶. That is to say, basis functions at different frequencies would be shifted by different amounts, resulting in shape changes (e.g. skewness) in the line profile. Therefore we modify the translation property of Fourier transform by rewriting x_0 as $x_0(\xi)$ in Eq. 2.3:

$$\Delta\phi(\xi) = -2\pi x_0(\xi)\xi. \quad (2.9)$$

As a result, the local gradient of the differential phase spectrum becomes

$$\frac{d(\Delta\phi)}{d\xi} = -2\pi(x_0 + \frac{dx_0}{d\xi}), \quad (2.10)$$

which reduces to Eq. 2.6 when x_0 is a constant as in the case of a bulk line shift. Note that the dependency of ξ has been taken out of $\Delta\phi(\xi)$ and $x_0(\xi)$ in writing the differential equation above.

In principle, we could numerically solve this differential equation based on the measured local gradient $d(\Delta\phi)/d\xi$ to obtain $x_0(\xi)$, but the local gradient measurement can be unreliable in the presence of noise. As a simplistic approach, we could use the *averaged* shift $\overline{x_0(\xi)}$ of various frequency modes to describe different amounts of shift by rewriting Eq. 2.9 as

$$\Delta\phi(\xi) = -2\pi\overline{x_0(\xi)}\xi \quad (2.11)$$

where $\overline{x_0(\xi)}$ is treated as a constant for the range of frequencies that we study. This concept will be helpful in describing the effective shifts applying the low-pass and high-pass filters when it comes to line deformation.

⁶excluding the case where the result of a line deformation is exactly the same as a line shift, as this becomes indistinguishable by any means of studying the shape of the line profile alone

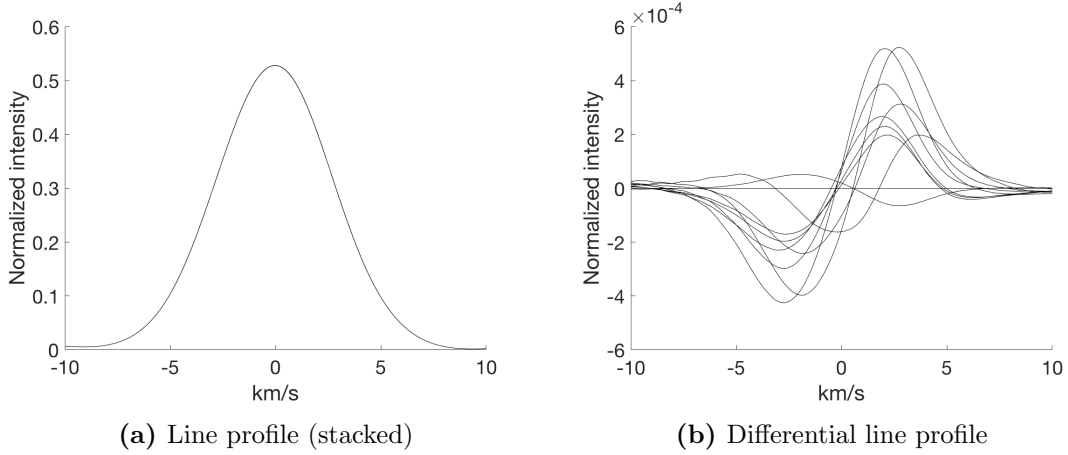


Fig. 2.8: Deformed line profile. For the sake of clarity, the differential line profiles are plotted noise-free and only 10 out of 100 profiles are presented.

2.2.2 SOAP simulations

In § 2.1, we had used the SOAP simulator only to generate a line profile that resembles the HARPS observation. In this section, we would use the simulator SOAP 2.0 to study line deformations arising from starspots.

Without loss of generality, we injected three spots with different longitudes, latitudes and sizes (parameters specified in Table 2.1) to model an emitting star, and generated 100 cross-correlation functions for the resulting deformed line profiles evenly sampled throughout the rotation period of the star (Fig. 2.8). A very small amount of noise (equivalent to a $S/N = 10,000$) was also added into the line profiles for simulation demonstration purposes.

	Longitude	Latitude	Size in disk area percentage
Spot 1	174°	-14°	0.18%
Spot 2	288°	74°	0.40%
Spot 3	51°	52°	0.50%

Table 2.1: Spot configurations

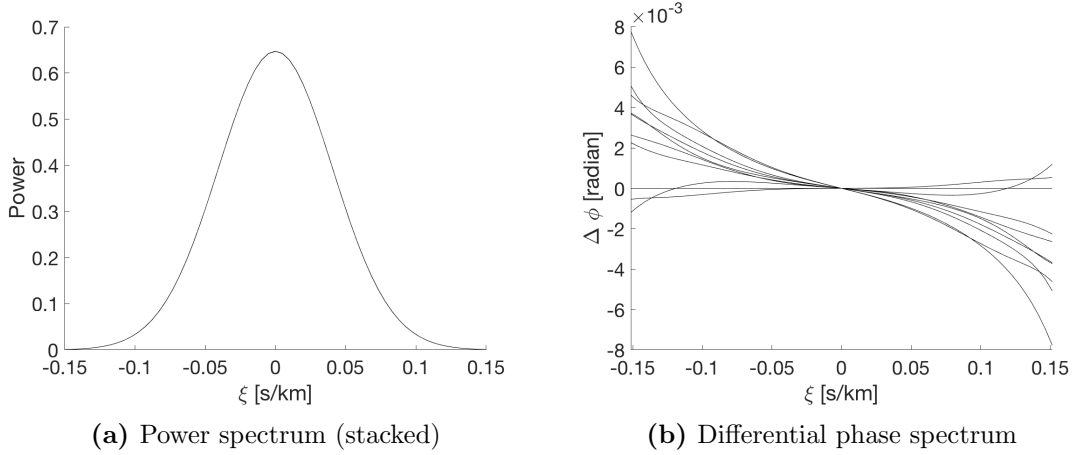


Fig. 2.9: Fourier transform of deformed line profile. Only 10 out of 100 differential phase spectra are presented.

2.2.3 Fourier phase spectrum analysis

2.2.3.1 RV_{FT}

We then take the same approach as in § 2.1 to obtain the power spectrum and the differential phase spectrum (Fig. 2.9) to recover the radial velocities RV_{FT} . It notes, line deformation contributes to a skewed differential phase spectrum, as predicted in §2.2.1.

In this case, the input radial velocities would be the apparent radial velocities of deformed line profiles (also known as jitter). Both velocities RV_{FT} and $RV_{Gaussian}$ are plotted against rotation phase (Fig. 2.10). If we take the root-mean-squares of both RV_{FT} and $RV_{Gaussian}$ to be the intrinsic noise level ($\sigma_{FT} = \sigma_{Gaussian} = 0.08$ m/s) corresponding $S/N = 10,000$, the uncertainty of $RV_{FT} - RV_{Gaussian}$ as residual would have an uncertainty of $\sqrt{\sigma_{FT}^2 + \sigma_{Gaussian}^2} \approx 0.11$ m/s. As $|RV_{difference}| = |RV_{FT} - RV_{Gaussian}| < 0.03$ m/s, we can agree that RV_{FT} and $RV_{Gaussian}$ are indistinguishably consistent.

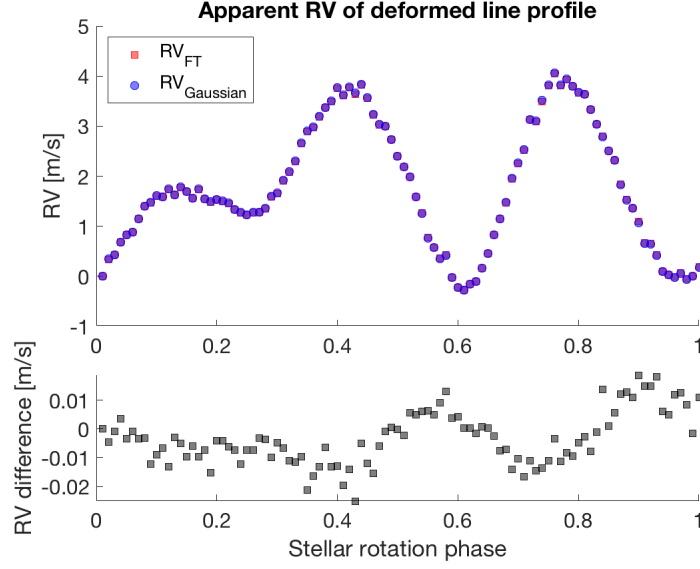


Fig. 2.10: Apparent RV of deformed line profile calculated with Fourier transform and Gaussian fit. Both results are also highly consistent with each other.
 $RV_{\text{difference}} = RV_{\text{FT}} - RV_{\text{Gaussian}}$.

To conclude, the Fourier phase spectrum analysis, using (almost) all the information in the power spectrum and the phase spectrum, returns highly consistent radial velocities as the line centroid acquiring by fitted a Gaussian profile. This consistency applies both for measuring a direct line shift and an apparent shift of a deformed line profile.

2.2.3.2 $RV_{\text{FT,H}}$ and $RV_{\text{FT,L}}$

Although the intrinsic line deformation (in the absence of any velocity shift in the host star) does mimic the radial velocity shift, we note the shape differences in the differential phase spectrum between an actual line shift (Fig. 2.3b) and a line deformation (Fig. 2.9b) – the latter presents relatively flat features in lower frequencies and becomes more skewed towards higher frequencies. Such differences provide key messages to differentiate the two circumstances.

According to §2.2.1 where we introduced $\overline{x_0(\xi)}$ – an averaged shift of a particular frequency range – we can therefore compute the equivalent radial velocity shift for each of the lower and higher frequency ranges (Fig. 2.11), denoted as $RV_{\text{FT,L}}$ and $RV_{\text{FT,H}}$ respectively.

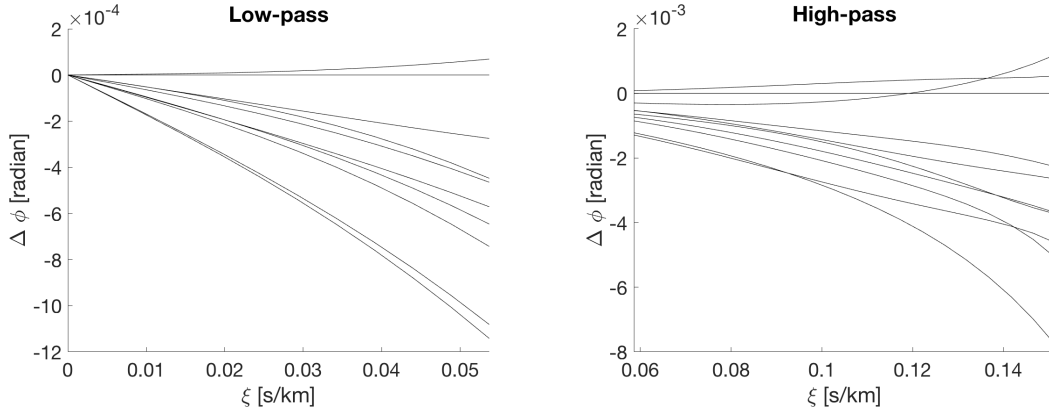


Fig. 2.11: Differential phase spectrum as shown in Fig. 2.9b sub-divided into lower frequency range and higher frequency range. Only the non-negative ranges are plotted.

To present our results, we plot the obtained $RV_{FT,L}$ and $RV_{FT,H}$ against the jitter (line centroid fitted by a Gaussian profile) in Fig. 2.12. The $RV_{FT,L}$ and $RV_{FT,H}$ can be clearly clustered into two groups, both linearly correlated with the jitter, and yet neither has a 1:1 correlation. $RV_{FT,H}$ demonstrates a higher response to jitter. Fitting with a linear regression model, it comes with a slope $k_H = 1.978 \pm 0.100$, meaning an apparent radial velocity shift of 1 m/s due to line deformation is detected as 1.978 ± 0.100 m/s shift on average using *this* high-pass filter; whereas the slope for applying a low pass filter is $k_L = 0.847 \pm 0.015$, meaning $RV_{FT,L}$ is less sensitive to the line profile deformation. When combining both filters, we would have obtained RV_{FT} , the same response to jitter, as shown in Fig. 2.10.

We could further investigate how well this linearity behaves for each filter by scaling the measured $RV_{FT,L}$ and $RV_{FT,H}$ by their corresponding factors $1/k_L$ and $1/k_H$ respectively, and compare them with the jitter (RV_{Gaussian}), as presented in Fig. 2.13. The root-mean-squares of the residuals ($RV_{FT,L/H}/k_{L/H} - RV_{\text{Gaussian}}$) are $\sigma_{FT,L} \approx 0.11$ m/s and $\sigma_{FT,H} \approx 0.31$ m/s respectively. The reason for $\sigma_{FT,H} > \sigma_{FT,L}$ is the same as mentioned in §2.1.5, being higher frequency modes are more affected by noise.

To conclude this subsection, the apparent radial velocity shift due to spectral line deformation (i.e. jitter) can be seen as a mingle of two radial velocities – $RV_{FT,H}$ and $RV_{FT,L}$ – one in higher frequency modes the other in lower frequency modes. They are both, as obtained from the simulated spectral line profiles, scaled linearly with jitter.

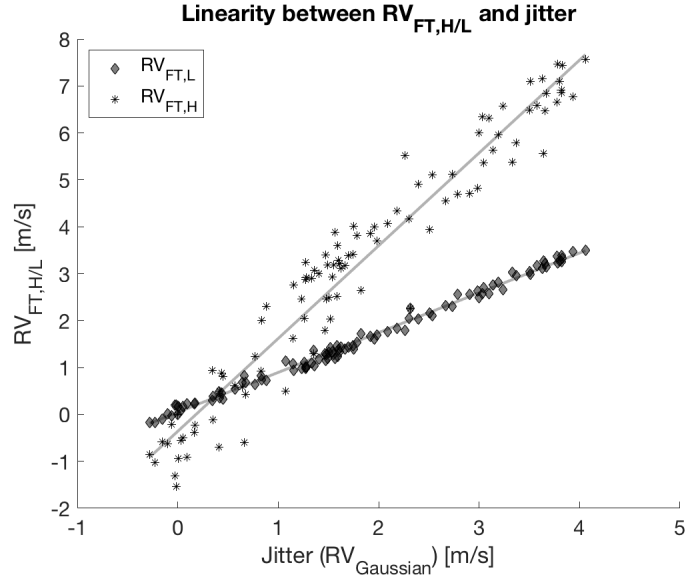


Fig. 2.12: Applying the low-pass and high-pass filters, the Fourier transform $RV_{FT,L}$ and $RV_{FT,H}$ are linearly correlated with the jitter ($RV_{Gaussian}$).

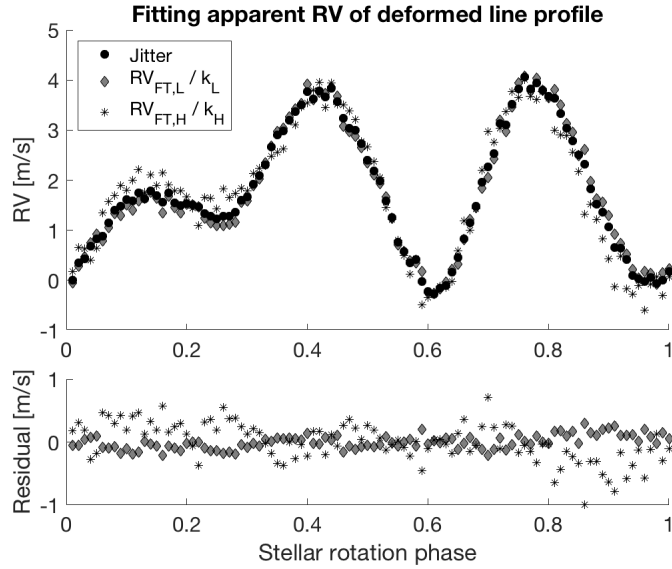


Fig. 2.13: Scaling the low-pass and high-pass Fourier transformed radial velocities to match the input jitter.

2.2.4 Jitter model

We have found in § 2.1 that the following measurable quantities demonstrate basically the same response to pure line shifts: RV_{FT} derived from the whole frequency range, $RV_{\text{FT,H}}$ from the higher frequency range, $RV_{\text{FT,L}}$ from the lower frequency range and RV_{Gaussian} being the line centroid fitted by a Gaussian profile. We have also found in this section (§ 2.2) so far, that both $RV_{\text{FT,H}}$ and $RV_{\text{FT,L}}$ are linearly correlated with the jitter, to which $RV_{\text{FT,H}}$ is more sensitive ($k_H > 1$) and $RV_{\text{FT,L}}$ is less sensitive ($k_L < 1$).

We can therefore write the following measurable quantities – RV_{Gaussian} (or RV_{FT}), $RV_{\text{FT,L}}$ and $RV_{\text{FT,H}}$ – as the sum of corresponding contributions from a bulk shift in the star (which we hereafter assume to be due to a planet or planets), and variability in the stellar line profile (hereafter lumped under the general name “jitter”)⁷:

$$RV_{\text{Gaussian}} = RV_{\text{planet}} + RV_{\text{jitter}} \quad (2.12)$$

$$RV_{\text{FT,L}} = RV_{\text{planet}} + k_L \cdot RV_{\text{jitter}} \quad (2.13)$$

$$RV_{\text{FT,H}} = RV_{\text{planet}} + k_H \cdot RV_{\text{jitter}}. \quad (2.14)$$

Subtracting one from the other to remove RV_{planet} and reduce to two independent equations

$$RV_{\text{Gaussian}} - RV_{\text{FT,L}} = (1 - k_L) \cdot RV_{\text{jitter}} \quad (2.15)$$

$$RV_{\text{FT,H}} - RV_{\text{Gaussian}} = (k_H - 1) \cdot RV_{\text{jitter}} \quad (2.16)$$

Rearranging yields two expressions of the jitter model

$$RV_{\text{jitter}} = \frac{RV_{\text{Gaussian}} - RV_{\text{FT,L}}}{1 - k_L} \quad (2.17)$$

$$RV_{\text{jitter}} = \frac{RV_{\text{FT,H}} - RV_{\text{Gaussian}}}{k_H - 1} \quad (2.18)$$

where RV_{Gaussian} , $RV_{\text{FT,L}}$ and $RV_{\text{FT,H}}$ are direct measurements, whereas k_L and k_H are unknowns⁸. Dividing the two equations above further cancels RV_{jitter} , leaving

$$\frac{RV_{\text{Gaussian}} - RV_{\text{FT,L}}}{RV_{\text{FT,H}} - RV_{\text{Gaussian}}} = \frac{1 - k_L}{k_H - 1}, \quad (2.19)$$

⁷For writing in elegance, a constant offset term for each of the equations is taken out in all of the following equations in this subsection.

⁸We could determine k_L and k_H in the demonstrated simulations only because we knew the jitter.

which means $(1 - k_L)/(1 - k_H)$ can now be robustly obtained by fitting a linear regression model on $(RV_{\text{Gaussian}} - RV_{\text{FT,L}})$ against $(RV_{\text{Gaussian}} - RV_{\text{FT,H}})$. With this, we rewrite the jitter model in a unified form – the weighted sum of the two jitter expressions from Eq. 2.17 and Eq. 2.18:

$$\begin{aligned}
 RV_{\text{jitter}} &= w_1 \frac{RV_{\text{Gaussian}} - RV_{\text{FT,L}}}{1 - k_L} + w_2 \frac{RV_{\text{FT,H}} - RV_{\text{Gaussian}}}{k_H - 1} \\
 &= \frac{1}{k_H - 1} \left[w_1 \frac{RV_{\text{Gaussian}} - RV_{\text{FT,L}}}{\frac{1 - k_L}{k_H - 1}} + w_2 (RV_{\text{FT,H}} - RV_{\text{Gaussian}}) \right] \\
 &= \alpha \left[w_1 \frac{RV_{\text{Gaussian}} - RV_{\text{FT,L}}}{\frac{1 - k_L}{k_H - 1}} + w_2 (RV_{\text{FT,H}} - RV_{\text{Gaussian}}) \right] \quad (2.20)
 \end{aligned}$$

in which the weights satisfy $w_1 + w_2 = 1$ and $1/(k_H - 1)$ is replaced by the scaling factor α in the last step.

Additionally, we can roughly estimate the uncertainty of RV_{jitter} in Eq. 2.17 and Eq. 2.18 by treating RV_{Gaussian} , $RV_{\text{FT,L}}$ and $RV_{\text{FT,H}}$ are independent variables, and $k_{L/H}$ is a constant:

$$\Delta RV_{\text{jitter,L}} \approx \frac{\sqrt{\sigma_{\text{Gaussian}}^2 + \sigma_{\text{FT,L}}^2}}{1 - k_L} \quad (2.21)$$

$$\Delta RV_{\text{jitter,H}} \approx \frac{\sqrt{\sigma_{\text{Gaussian}}^2 + \sigma_{\text{FT,H}}^2}}{k_H - 1}. \quad (2.22)$$

Substituting the following values: $\sigma_{\text{Gaussian}} = 0.08$ m/s (§2.1.4), $\sigma_{\text{FT,L}} = 0.11$ m/s and $\sigma_{\text{FT,H}} = 0.43$ m/s (§2.1.5), $k_L = 0.847$ and $k_H = 1.978$ (§2.2.3.2), we obtain $\Delta RV_{\text{jitter,L}} = 0.89$ m/s and $\Delta RV_{\text{jitter,H}} = 0.45$ m/s.

When there's no planet or the planetary radial velocity signal is negligible compared with the size of jitter, $RV_{\text{FT,L}}$ and $RV_{\text{FT,H}}$ will be proportional to RV_{jitter} (Example: §2.3.1).

2.2.5 Testing the recovery of jitter

We again performed tests to see if we can correctly recover artificially generated jitter using our new technique (Eq. 2.20).

We generated 200 deformed line profiles (in the form of cross-correlation functions) using SOAP 2.0. All the configurations are the same as used in §2.2.2, except that the data are produced from two rotation periods instead of one. The jitter amplitude is

roughly 2 m/s. In addition, each line profile is further shifted by an amount RV_{planet} appropriate for a planet generating a Keplerian orbit in the star of the amplitude⁹: $A_{\text{planet}} = 2$ m/s. The planetary orbital period to stellar rotation period ratio is set to be 0.7 (i.e. $P_{\text{rot}}/P_{\text{orb}} = \nu_{\text{orb}}/\nu_{\text{rot}} = 0.7$).

We then obtain three sets of radial velocities for each simulated profile: RV_{Gaussian} , $RV_{\text{FT,H}}$ and $RV_{\text{FT,L}}$ (Fig. 2.14 upper panel). We test three different combinations of w_1 and w_2 and apply a scaling factor α (fitted by linear regression to the known input jitter) to see how well it matches the input jitter: (1) $w_1 = 1, w_2 = 0$; (2) $w_1 = 0.5, w_2 = 0.5$; (3) $w_1 = 0, w_2 = 1$. To visually show the trends of these three test jitter models, a moving average modulated by a Gaussian kernel is implemented to smooth out the data (Fig. 2.14 middle panel). All these three sets of jitter model successfully recover adequate information of the input jitter, while presenting minor difference among each other.

To quantitatively examine their performance, we compare the scatter of the input jitter σ_{jitter} and that of the difference between the input jitter and the jitter models σ_{residual} . The former can be treated as the scatter after fitting the correct planet(s) without jitter correction, while the latter can be treated as the scatter after the additional jitter is removed. Table 2.2 lays out the scatter σ_{residual} for the raw jitter models and the smoothed jitter models. The smoothed jitter can be useful in reducing the larger scatter of radial velocities obtained directly from the Fourier transform, especially in lower S/N observations. In addition to the nearly noise-free (S/N=10,000) simulations, the corresponding results for real-world observations are presented in parallel. For example, S/N ranging from 2,000 to 4,000 is found in HARPS cross-correlation functions of spectral line profiles for a dwarf star HD 189733, whose apparent magnitude is $V = 7.6$; S/N \sim 1,000 is found for red dwarfs Gl 176 and Wolf 1061, of which $V \sim 10$. We choose S/N=2,000 for demonstration in the table.

	σ_{residual} (raw) [m/s]		σ_{residual} (smoothed) [m/s]	
	S/N=10,000	S/N=2,000	S/N=10,000	S/N=2,000
$w_1 = 1, w_2 = 0$	0.69	2.49	0.54	0.65
$w_1 = 0.5, w_2 = 0.5$	0.78	2.59	0.62	0.75
$w_1 = 0, w_2 = 1$	0.72	2.42	0.51	0.68

Table 2.2: Scatter of jitter residual

⁹In principle, the RV_{planet} configuration shouldn't matter in producing the jitter model because it is cancelled out in the jitter model as derived in §2.2.4.

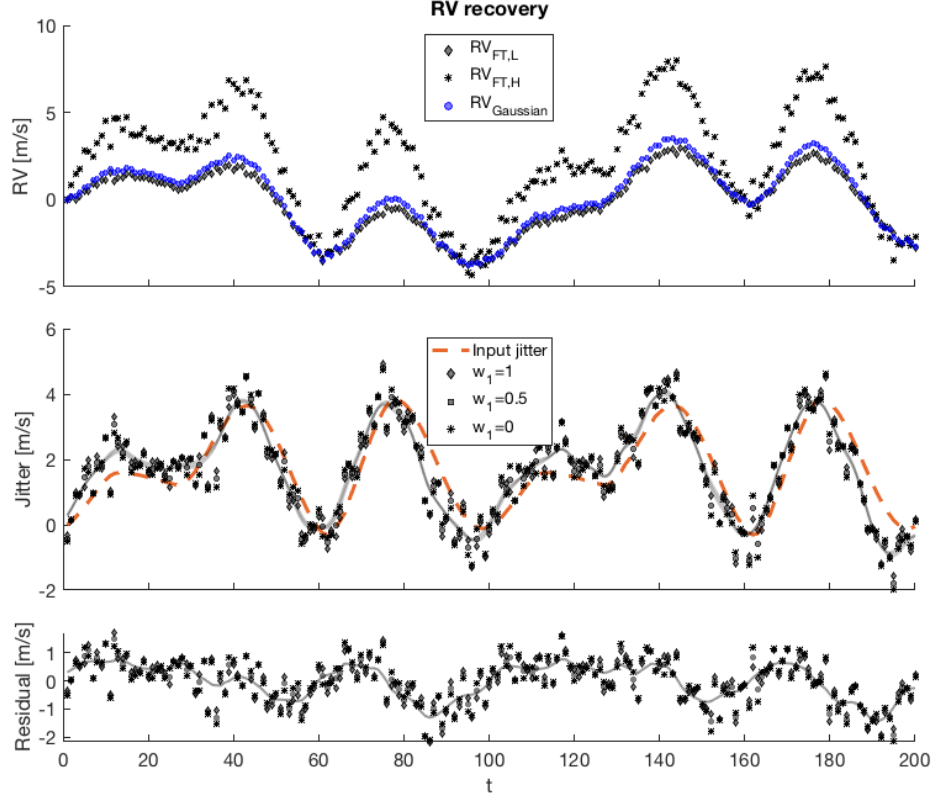


Fig. 2.14: Construct jitter model from simulation data.

The scatter of the input jitter is $\sigma_{\text{jitter}} = 1.22$ m/s, effectively reduced to $\sigma_{\text{residual}} = 0.70$ m/s for $S/N=10,000$ but conversely doubled for $S/N=2,000$. Applying proper smoothing¹⁰ can reduce the input jitter scatter σ_{jitter} by half in both cases. This is crucial in enhancing the detection of planets with radial velocities of sub-m/s amplitudes. However, we should also note that there can be systematic differences between the input jitter and our jitter models that occurs in the rotational period of the star.

2.2.6 Planetary radial velocity recovery

Having obtained the jitter model (Eq. 2.20) and knowing RV_{planet} follows a Keplerian orbital motion, we can turn our planetary radial velocity recovery into a model fitting problem, in which the parameters of the jitter model (such as the scaling factor) and

¹⁰Specifically speaking, we take into account the correlations among data points close to each other, by applying a moving average modulated by a Gaussian kernel. Other smoothing techniques such as the use of the Python package PyMC3 that implements Gaussian process in smoothing the data also return similarly good results.

that of the Keplerian orbit (such as amplitude, orbital period and phase) are to be determined.

Alternatively, we can bypass the jitter model. Revisiting the Equations 2.12-2.14, we rewrite them by observation number i ($i = 1, 2, \dots, N$) and switch the notations to obtain the following $3N$ independent linear equations:

$$X_i = P_i + J_i \quad (2.23)$$

$$Y_i = P_i + k_y \cdot J_i \quad (2.24)$$

$$Z_i = P_i + k_z \cdot J_i \quad (2.25)$$

where X_i, Y_i and Z_i replace the three measurable radial velocities RV_{Gaussian} , $RV_{\text{FT,L}}$ and $RV_{\text{FT,H}}$; P_i and J_i are the planetary radial velocities and the jitter; k_y and k_z are the scaling factors k_L and k_H . Substituting $J_i = X_i - P_i$ from Eq. 2.23, we can simply the system to the following $2N$ independent linear equations:

$$Y_i = k_y \cdot X_i + (1 - k_y)P_i \quad (2.26)$$

$$Z_i = k_z \cdot X_i + (1 - k_z)P_i. \quad (2.27)$$

The number of unknowns is $(N+4)$, including N from P_i , 2 from k_y and k_z , and another 2 from the previously omitted constant offsets. Normally we have $N \gg 1$, so that the number of independent equations ($2N$) is larger than the number of degrees of freedom ($N+4$) in the system, meaning the system can be uniquely solved by optimization, such as least square minimization of the objective function:

$$\sum_{i=1}^N \left[w_{y,i} \left(k_y \cdot X_i + (1 - k_y)P_i - Y_i \right)^2 + w_{z,i} \left(k_z \cdot X_i + (1 - k_z)P_i - Z_i \right)^2 \right] \quad (2.28)$$

where $w_{y,i}$ and $w_{z,i}$ are pre-determined parameters (e.g. determined by the sizes of errorbars of the observed radial velocities) used to weight the linear systems. In addition, this approach becomes identical to constructing a jitter model (Eq. 2.20) in cases that (1) $w_{y,i} = 1, w_{z,i} = 0$ ($i = 1, 2, \dots, N$) and $w_1 = 1, w_2 = 0$; (2) $w_{y,i} = 0, w_{z,i} = 1$ ($i = 1, 2, \dots, N$) and $w_1 = 0, w_2 = 1$.

2.2.7 End-to-end simulations

In this subsection we will be testing three categories of determining a planet candidate in the presence of jitter through end-to-end simulations:

1. In a system where the amplitude of jitter is comparable to that of the planetary radial velocities, can we recover the planet orbital parameters better with our Fourier phase analysis than without jitter correction?
2. In a system where the planetary radial velocities dominate and jitter is negligible, does our method give at least equally good results as the traditional methods?
3. In a system where jitter is the only source of radial velocities, can our method inform us about it?

We will also answer the important question: how to classify these three categories in the first place?

The spectral line profile simulator setup is the same as previously, except setting S/N to be 2,000 to imitate a real-world cross-correlation function of a line profile from HARPS. The jitter amplitude is fixed at roughly 2 m/s, so we will adjust the planetary orbital amplitude to satisfy these three categories. We will run 200 trails, each trail with 60 randomly selected samples clustered in 12 groups, out of a total of 400 equally spaced samples from four stellar rotation periods.

The tests are divided into two main groups for comparison:

1. Fit RV_{Gaussian} by Keplerian orbit alone;
2. Fit RV_{Gaussian} by Keplerian orbit with jitter model correction. The following three variations of model fitting have been tested:
 - (a) Jitter model constructed with RV_{Gaussian} and $RV_{\text{FT,L}}$ only, i.e. $w_1 = 1$ and $w_2 = 0$;
 - (b) Jitter model constructed with RV_{Gaussian} and $RV_{\text{FT,H}}$ only, i.e. $w_1 = 0$ and $w_2 = 1$;
 - (c) Jitter model constructed with RV_{Gaussian} , $RV_{\text{FT,L}}$ and $RV_{\text{FT,H}}$. We test with $w_1 = 0.5$ and $w_2 = 0.5$;

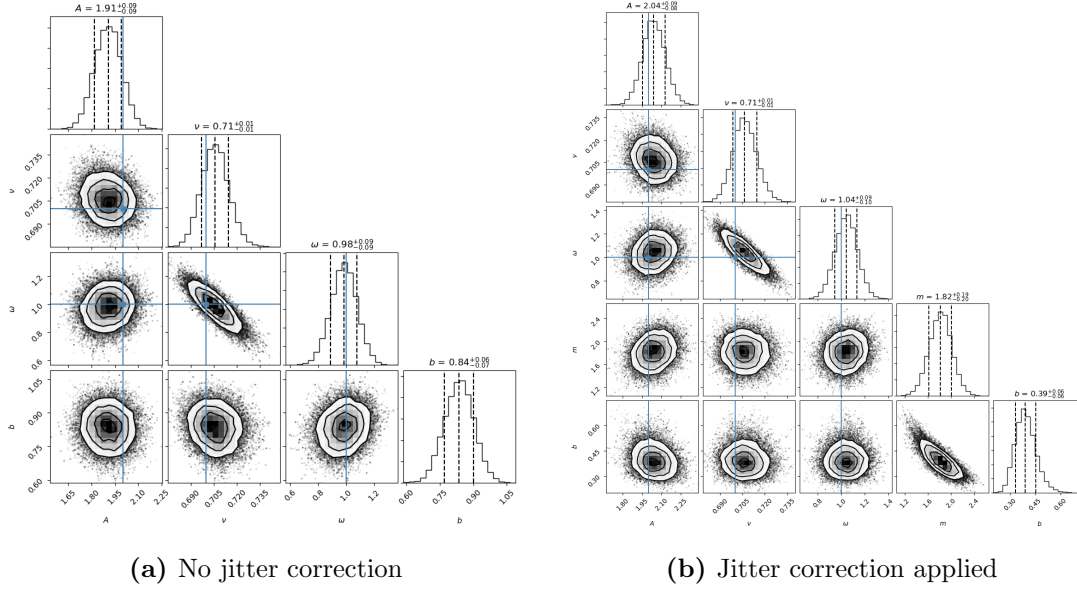


Fig. 2.15: Examples of two corner plots showing the successfully recovered planetary orbital parameter with MCMC sampling. The blue solid lines indicate the true values of the input orbital parameters. The three dashed lines of each histogram indicate the median and 1σ on both sides.

The parameters for the fitting is obtained by Markov chain Monte Carlo (MCMC) sampling. Each radial velocity data is equally weighted as they have the same S/N. We find that among the three variations of jitter correction treatments, the one left with the least rms statistically returns the best parameter fitting performance, so we will choose the one to represent the fitting from Group2.

2.2.7.1 Stellar jitter as strong as planetary signal

The injected planet has the same parameter settings as in §2.2.5, i.e. circular orbit with amplitude $A = 2$ m/s, orbital frequency ratio $\nu = \nu_{\text{orb}}/\nu_{\text{rot}} = 0.7$ and initial phase $\omega = 1$ rad. After running for 200 trails, we recover the parameters for each trail (Fig. 2.15) and obtain the histograms of the recovered orbital parameters, e.g. the amplitude and the orbital period (here the orbital frequency ratio) that we mostly concerned about (Fig. 2.17).

To quantitatively describe their performances, we calculate the percentage of parameters successfully recovered within 5% and 10% of the true values as summarized in Table 2.3. For example, 15% of the 200 trails have both the amplitude (A) and orbital frequency ($\nu_{\text{orb}}/\nu_{\text{rot}}$) successfully recovered within 5% of the true parameters with

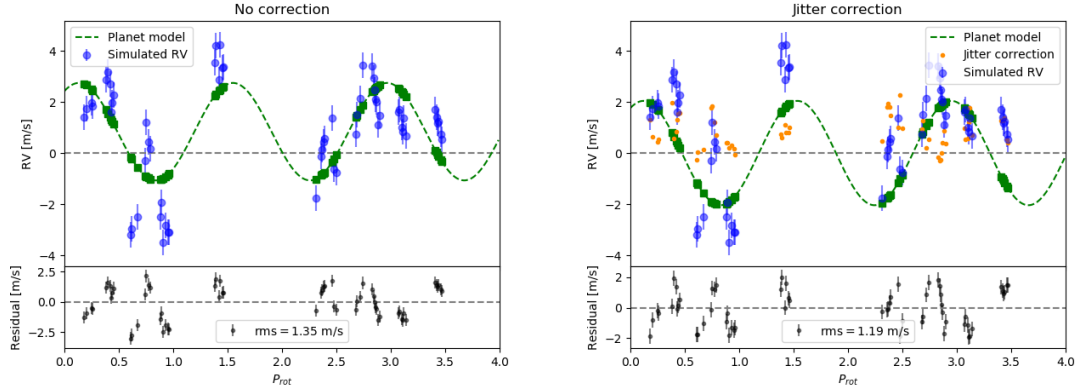


Fig. 2.16: Radial velocity fitting. These are two fittings that comes out from the MCMC corner plots in Fig. 2.15 on the same set of simulated radial velocities. The discrepancy between the simulated radial velocities and the planet model is accounted for by the jitter model, and thus applying the jitter correction reduces the rms of the residual.

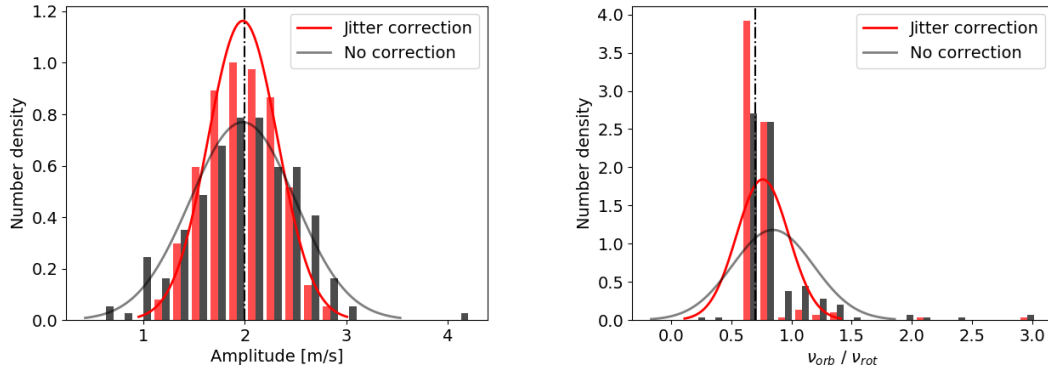


Fig. 2.17: Histogram of recovered orbital parameters with a Gaussian profile fitted on top. The results from jitter correction are labelled in red (left in the histogram and dark in the Gaussian profile) and that without correction are labelled in grey (right in the histogram and light the Gaussian profile).

jitter correction applied, while only 8% of them achieve such a precision without jitter correction.

Percentage	5% limit		10% limit	
	†	‡	†	‡
A	16%	23%	32%	39%
$\nu_{\text{orb}}/\nu_{\text{rot}}$	40%	58%	67%	89%
both A and $\nu_{\text{orb}}/\nu_{\text{rot}}$	8%	15%	23%	37%

Table 2.3: Proportion of recovered parameters within a 1% or 5% limit of $A = 2$ m/s and $\nu_{\text{orb}}/\nu_{\text{rot}} = 0.7$. †: no correction; ‡: jitter correction applied.

2.2.7.2 Planetary signal dominates

In this case, we set the orbital amplitude roughly 10 times as strong as the jitter, i.e. $A = 20$ m/s (Fig. 2.18). This scenario hardly has impact on obtaining high precision of the orbital parameters of the planets using both approaches (Fig. 2.19), but applying jitter correction slightly improves the performance with an overall more precise measurements of the orbital parameters (Table. 2.4).

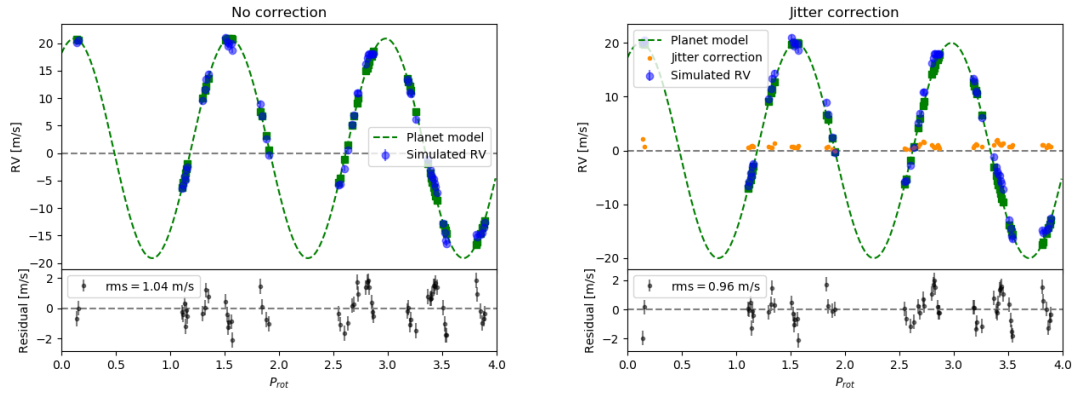


Fig. 2.18: Same with Fig. 2.16 except the input orbital amplitude of the planet being $A = 20$ m/s.

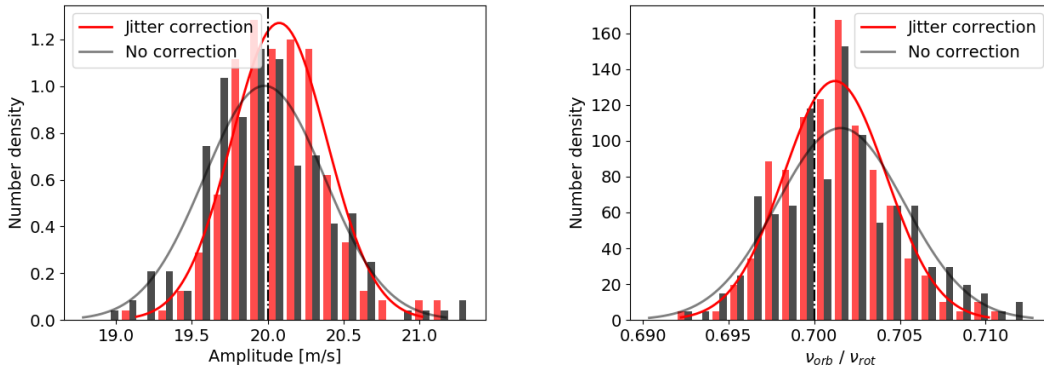


Fig. 2.19: Same with Fig. 2.17 except the input orbital amplitude of the planet being $A = 20$ m/s.

Percentage	1% limit		5% limit	
	†	‡	†	‡
A	41%	51%	98%	99%
$\nu_{\text{orb}}/\nu_{\text{rot}}$	91%	97%	100%	100%
both A and $\nu_{\text{orb}}/\nu_{\text{rot}}$	37%	49%	98%	99%

Table 2.4: Proportion of recovered parameters within a 5% or 10% limit of $A = 20$ m/s and $\nu_{\text{orb}}/\nu_{\text{rot}} = 0.7$. †: no correction; ‡: jitter correction applied.

2.2.7.3 Stellar jitter only

We set $A = 0$ m/s so that the measured the radial velocity only comes from stellar variability. We implement the same approaches as above to see if the applying the jitter correction can return a null planet solution i.e. recovered amplitude smaller than the noise level.

The input jitter is the same as used in Fig. 2.13, showing the presence of three starspots in turns, mimicking the radial velocities of orbiting exoplanets. This is indeed the case in the histogram of “recovered” orbital parameters (Fig. 2.20): $\nu_{\text{orb}}/\nu_{\text{rot}}$ pops up at around 1, 2 and 3, with 3 being the most prominent.

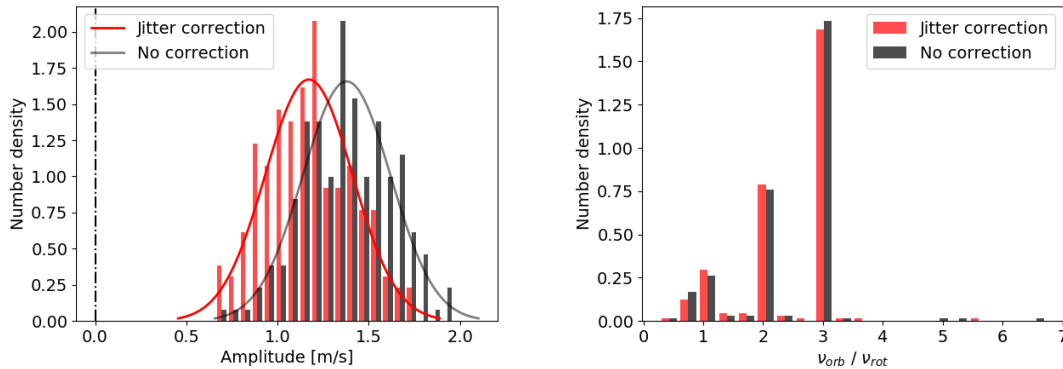


Fig. 2.20: Histogram of “recovered” orbital parameters of null planets.

2.3 Fourier transform with real observations

2.3.1 HD189733: Rossiter–McLaughlin effect as jitter

HD189733 is a well studied binary star system. The main star HD189733 A is known to host a gas giant exoplanet HD189733 b, first detected by transits (reference...) and later

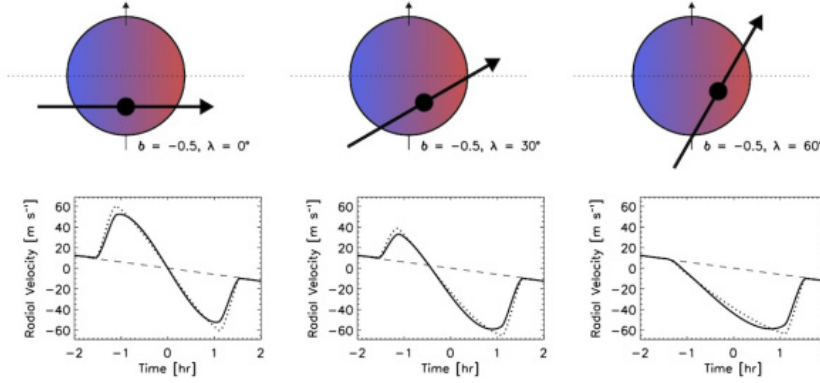


Fig. 2.21: Demo: Rossiter–McLaughlin effect (reference...). It is an apparent radial velocity change of the parent star due to an eclipsing binary (whether star or planet) that breaks the observed flux symmetry in the stellar photosphere, resulting in imbalanced redshift and blueshift. It shows in this plot three different star-planet alignments that cause three corresponding different shapes of radial velocity curve, and hence the radial velocity curve sheds information on the geometry of the alignment.

by Doppler spectroscopy (references...). It was also the first exoplanet transit observed in X-ray (references...).

We choose this target for the following reasons:

- The exoplanet is well confirmed;
- The host star is bright enough: $m_V = 7.66$;
- The gas giant exoplanet causes a prominent apparent radial velocity while it transits (~ 40 m/s) due to Rossiter–McLaughlin effect.

We treat as if it were an “active” star with one big dark starspot, as the Rossiter–McLaughlin effect causes the line profile deformed in a similar manner that a starspot would do (Fig. 2.21). We aim to test if our jitter model can account for the radial velocity variation from Rossiter–McLaughlin effect.

The procedure is rather standardized. Both RV_{Gaussian} and RV_{FT} are calculated from the HARPS cross-correlation functions of the spectra. $\Delta RV = RV_{\text{Gaussian}} - RV_{\text{FT}}$ are then smoothed by a Gaussian filter. The prototype of the Rossiter–McLaughlin radial velocity curve is already identifiable (ΔRV of the lower panel of Fig. 2.22).

During transit, as the parent star and the exoplanet are along the line of sight, there will be no contribution to radial velocity by the orbiting exoplanet. However, the

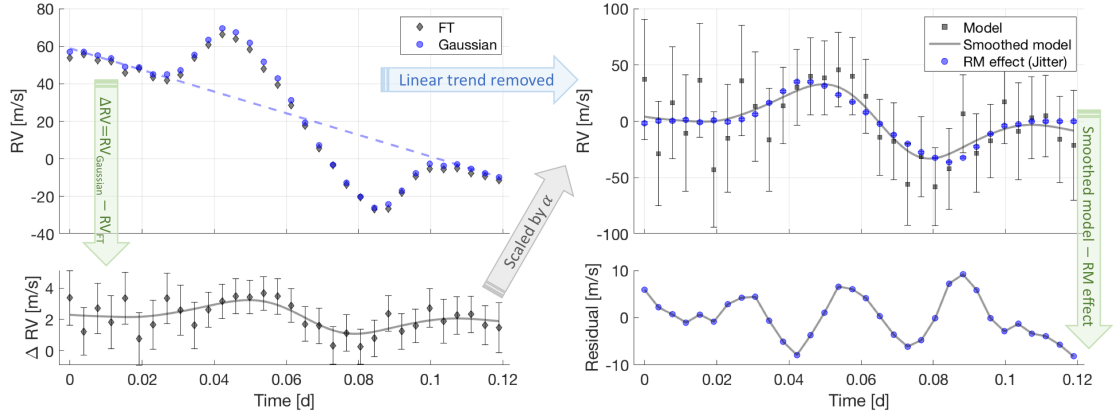


Fig. 2.22: HD189733: removal of Rossiter–McLaughlin effect as jitter. From RV_{Gaussian} and RV_{FT} to ΔRV . The scattered ΔRV are smoothed by applying a moving average with a Gaussian filter and further weighted according to the size of errorbar. It is then scaled by α to match the jitter (in this case the radial velocities of the observed Rossiter–McLaughlin effect). The residual is the difference between the smoothed jitter model and the observed Rossiter–McLaughlin effect. Errorbars are not plotted for the residuals for the reason that they will overwhelm the residual themselves.

radial velocity shows an inclined trend in this system. It is due to the other orbiting star in the binary star system. Considering the orbital period of the binary star estimated around 3,200 years (reference...), the radial velocity contribution from the other star during the timespan of transit (~ 0.08 days) can be treated linear. By removing such a linear trend, which is fitted for the non-transiting part, we can extract the observed Rossiter–McLaughlin radial velocity curve. It is treated as jitter and modelled by $\alpha \cdot \Delta RV$ (Fig. 2.22 upper right). Note that the errorbars of the jitter model also becomes a factor of α ($\alpha \gg 1$) larger; however, the model itself shows a descent approximation of the Rossiter–McLaughlin radial velocity curve. The difference between our modelled jitter and the observed Rossiter–McLaughlin effect peaks at ~ 10 m/s, a $\sim 75\%$ removal of the jitter from ~ 40 m/s.

Remarks The effective length of the smoothing kernel should be carefully chosen. In this case, it's chosen most effective within roughly one neighbouring data point on both size. While mitigating the effect of noise (especially for relatively lower S/N data outside the transits), to which the Fourier transform is sensitive, it also smears the drastic velocity change when the planet ingresses and egresses the stellar disk. To solve this awkward situation, an adaptive (i.e. S/N dependent) effective length of the smoothing kernel may be used.

2.3.2 Examples 2

HD 49933 is an F2 main sequence star with an apparent magnitude of $m_V = 5.8$ ([2]),

2.3.3 Example 3

A float barrier will stop figures from going beyond this point. They are handy to make sure they don't go into the next section.

2.4 References

- [1] X. Dumusque, I. Boisse, and N. C. Santos. Soap 2.0: A tool to estimate the photometric and radial velocity variations induced by stellar spots and plagues. *The Astrophysical Journal*, 796(2):132, 2014. 7
- [2] S. Malaroda. Study of the F-type stars. I. MK spectral types. *aj*, 80:637–641, August 1975. 32